Accelerated 2D Real-Time Refraction-Corrected Transcranial Ultrasound Imaging

Mozaffarzadeh, M.; Verschuur, D.J.; Verweij, M.D.; de Jong, N.; Renaud, G.G.J.

DOI
10.1109/TUFFC.2022.3189600

Publication date
2022

Document Version
Final published version

Published in
IEEE Transactions on Ultrasonics, Ferroelectrics and Frequency Control

Accelerated 2-D Real-Time Refraction-Corrected Transcranial Ultrasound Imaging

Moein Mozaffarzadeh, Dirk J. Eric Verschuur, Martin D. Verweij, *Member, IEEE*, Nico de Jong, *Member, IEEE*, and Guillaume Renaud

***Abstract*— In a recent study, we proposed a technique to correct aberration caused by the skull and reconstruct a transcranial B-mode image with a refraction-corrected synthetic aperture imaging (SAI) scheme. Given a sound speed map, the arrival times were calculated using a fast marching technique (FMT), which solves the Eikonal equation and, therefore, is computationally expensive for real-time imaging. In this article, we introduce a two-point ray tracing method, based on Fermat's principle, for fast calculation of the travel times in the presence of a layered aberrator in front of the ultrasound probe. The ray tracing method along with the reconstruction technique is implemented on a graphical processing unite (GPU). The point spread function (PSF) in a wire phantom image reconstructed with the FMT and the GPU implementation was studied with numerical synthetic data and experiments with a bone-mimicking plate and a sagittally cut human skull. The numerical analysis showed that the error on travel times is less than 10% of the ultrasound temporal period at 2.5 MHz. As a result, the lateral resolution was not significantly degraded compared with images reconstructed with FMT-calculated travel times. The results using the synthetic, bone-mimicking plate, and skull dataset showed that the GPU implementation causes a lateral/axial localization error of 0.10/0.20, 0.15/0.13, and 0.26/0.32 mm compared with a reference measurement (no aberrator in front of the ultrasound probe), respectively. For an imaging depth of 70 mm, the proposed GPU implementation allows reconstructing 19 frames/s with full synthetic aperture (96 transmission events) and 32 frames/s with multiangle plane wave imaging schemes (with 11 steering angles) for a pixel size of 200 μm. Finally, refraction-corrected power Doppler imaging is demonstrated with a string phantom and a bone-mimicking plate placed between the probe and the moving string. The proposed approach achieves a suitable frame rate for clinical scanning while maintaining the image quality.**

***Index Terms*— Adaptive beamforming, graphical processing unite, phase aberration correction, temporal bone, transcranial ultrasound imaging (TUI).**

I. Introduction

REAL-TIME ultrasound imaging of the brain started in the late sixties with the development of the first electronic two-dimensional (2-D) scanner developed by Somer [1]. Decades after, transcranial ultrasound imaging (TUI) remains very challenging and offers poor image quality compared with ultrasound imaging of many body regions where no ultrasound propagation through bone occurs. Poor image quality of TUI results from strong wave aberration [2] and multiple scattering caused by the skull [3], [4]. Current commercial TUI devices ignore the skull.

TUI is nowadays available in most hospitals, clinics, and emergency medicine services (EMSs) worldwide [5]–[8]. Compared with CT and MRI, ultrasound imaging is safe (nonionizing), portable (can be used at bed-site and EMS), and relatively inexpensive. Despite its poor image quality, TUI was shown to be useful for the diagnosis of stroke [8]–[14], prevention of stroke in children (between an age of 2 and 16) with sickle cell disease [15]–[17], and vasospasm detection after subarachnoid hemorrhage [18], [19].

TUI is often performed through the temporal window (the thinnest part of the skull that gives the most optimal ultrasound access to the brain) where the squamous part of the temporal bone often consists of a single layer of cortical bone [20]–[23]. Phase aberration correction was first proposed by modeling the temporal bone as an infinitesimally thin aberrating layer at the surface of the transducer (the so-called the near-field phase-screen aberration model) [24]–[26], but the correction obtained by this approach is limited (axially and laterally) to a certain region called the isoplanatic patch [3], [27]–[30]. Another approach is using either ultrasound measurements [31]–[33] or CT/MRI scans of the skull to obtain the true geometry and sound speed of the temporal bone prior to image reconstruction, and then correct phase aberration and refraction during image reconstruction [34]–[37]. Recently, we have shown the feasibility of single-sided 2-D transcranial ultrasound through the human temporal window using a single handheld commercial probe, where the position, true geometry,

Manuscript received 18 May 2022; accepted 6 July 2022. Date of publication 7 July 2022; date of current version 30 August 2022. This work was supported by a joint grant from the Netherlands Organization for Scientific Research (NWO)/the Netherlands Organization for Health Research and Development (ZonMw) and the Department of Biotechnology (Government of India) under the Program Medical Devices for Affordable Health (MDAH) as Project Imaging Needles under Grant 116310008. *(Corresponding author: Moein Mozaffarzadeh.)*

Moein Mozaffarzadeh and Guillaume Renaud are with the Laboratory of Medical Imaging, Department of Imaging Physics, Delft University of Technology, 2628 CJ Delft, The Netherlands (e-mail: m.mozaffarzadeh@tudelft.nl).

Dirk J. Eric Verschuur is with the Department of Imaging Physics, Section of Computational Imaging, Delft University of Technology, 2628 CJ Delft, The Netherlands.

Martin D. Verweij and Nico de Jong are with the Laboratory of Medical Imaging, Department of Imaging Physics, Delft University of Technology, 2628 CJ Delft, The Netherlands, and also with the Department of Biomedical Engineering, Thorax Center, Erasmus Medical Center, 3015 GD Rotterdam, The Netherlands.

This article has supplementary downloadable material available at https://doi.org/10.1109/TUFFC.2022.3189600, provided by the authors.

Digital Object Identifier 10.1109/TUFFC.2022.3189600

and sound speed of the bone layer were estimated for an accurate correction of phase aberration and refraction [38], [39]. The same methodology was used before for *in vivo* imaging of the inner structure of the radius and tibia bone [40], [41]. While promising results were achieved, no fast-enough implementation is available for real-time transcranial imaging, i.e., enabling an imaging rate of at least 20 images/s, which limits its application in practice, especially for translation to 3-D TUI [38], [42]–[44]. Real-time image reconstruction is essential in practice as it allows the operator to freely move the probe find the proper imaging window and imaging plane, and look for biomarkers related to a possible brain disorder in either B-mode or flow images. A frame rate of 4 Hz was reported in [41], but still not fast enough for real-time visualization.

Over the past two decades, the emergence of graphical processing unites (GPUs) has facilitated high-performance computing [45]–[47]. Medical ultrasound imaging also took advantage of this technology [48]–[50]. Different beamforming techniques such as Capon [49], [51]–[53], short-lag spatial coherence [50], [54]–[56], synthetic aperture sequential beamforming [57], [58], delay-multiply-and-sum [59] and double-stage delay-multiply-and-sum [60], [61], and volumetric imaging systems [62]–[64] were accelerated by GPU. GPU-based beamforming softwares were developed [65], [66], and ultrasound vector flow imaging systems were accelerated [67]–[69]. Yiu *et al.* [70] reported on a very high frame rate realization of the synthetic aperture and multi-angle plane wave imaging schemes with two GPUs and a recursive implementation, which can output between 1000 and 5000 frames/s depending on the number of receive channels and image depth.

Despite all the acceleration achieved by GPUs in medical ultrasound imaging field, implementations are all based on a strong assumption: an imaging medium with a constant wave-speed (∼1540 m/s). This does not apply to TUI. In this article, we introduce an accelerated image reconstruction technique that corrects for phase aberration and wave refraction caused by the human temporal bone for real-time imaging. The two-point ray tracing concept (introduced by Waltham [44]) was used to find the shortest (following Fermat's principle) travel time connecting an image pixel to an array element or a virtual point source (for diverging or plane wave imaging) [71]. Unlike in [40] and [41], the approach is not iterative and the near and far surfaces of the bone layer are described in a discrete manner using the image grid points. This allows a faster calculation of the travel times and, therefore, tremendously reduces computational time for image reconstruction. Its implementation on a GPU further reduces computational time.

II. Accelerated Ray-Tracing-Based Reconstruction

A. Principle of the Proposed Method

Image reconstruction is most often performed with a delay-and-sum algorithm, which requires the accurate calculation of the ultrasound round-trip travel times (i.e., from the source to the image pixel and from the image pixel back to the array elements). Several techniques exist to calculate these travel times in a layered medium. Eikonal solvers propagate the wavefront through the medium to calculate the travel time from an array element or a virtual point source to an image pixel in the brain region [38], [41]–[43]. Another approach is iterative two-point ray tracing, where the ray path providing the minimum travel time (Fermat's principle) is searched iteratively and accurately using a method for function minimization, for instance, a ray bending approach using Brent's algorithm [39]–[41]. However, Eikonal solvers and iterative two-point ray tracing are too computationally expensive to reconstruct more than 20 images/s. In contrast, our approach is less accurate but much faster because it seeks the shortest travel times by evaluating the travel time for a limited number of possible ray paths passing through a limited number of intermediate points (IPs). IPs are defined as the image pixels describing the near and far surfaces of the bone layer in the image. The terms "near surface" and "far surface" are defined with respect to the probe. A summary of the proposed accelerated ray-tracing-based imaging approach is provided in Fig. 1. We propose the following three steps to reconstruct a refraction-corrected image.

1) The pixels on the far surface of the silicone rubber front layer in the transducer are defined as IPs (SIPs; the red squares in Fig. 1).
   The ray tracing starts to find the shortest travel time from pixels in the skin [up to a certain maximum depth where we expect to detect the near surface of the bone, see the red dashed line in Fig. 1(a)] to each array element through the SIPs; see the red vectors in Fig. 1(a). The sound speed of the skin should be used to convert the distance into travel time. The image is reconstructed within the skin area up to the maximum expected depth of the near surface of the skull and using the estimated travel times. Thus, the image contains the near surface of the bone layer, which is then segmented using Dijkstra's algorithm [72]. This algorithm seeks the path that crosses the image from left to right and follows the image pixels with the highest intensity in the ultrasound image, by maximizing a merit; here, the sum of the pixel values along the path is used.
2) The IPs are updated (called NIPs) to the pixels on the segmented near surface [see the black squares in Fig. 1(b)]. The ray tracing finds the shortest travel time from pixels in the bone (up to a certain maximum depth where we expect to detect the far surface of the bone [see the black dashed line in Fig. 1(b)]) to each array element through the NIPs; the black vectors in Fig. 1(b) are examples of the paths. The compressional wave speed of the bone should be used to convert the distances into travel times. The image is reconstructed up to the maximum expected depth of the far surface of the skull and using the estimated travel times. The far surface of the bone layer is segmented using Dijkstra's algorithm.
3) The IPs are updated along the far surface of the bone layer [called FIPs; see the purple squares in Fig. 1(c)].

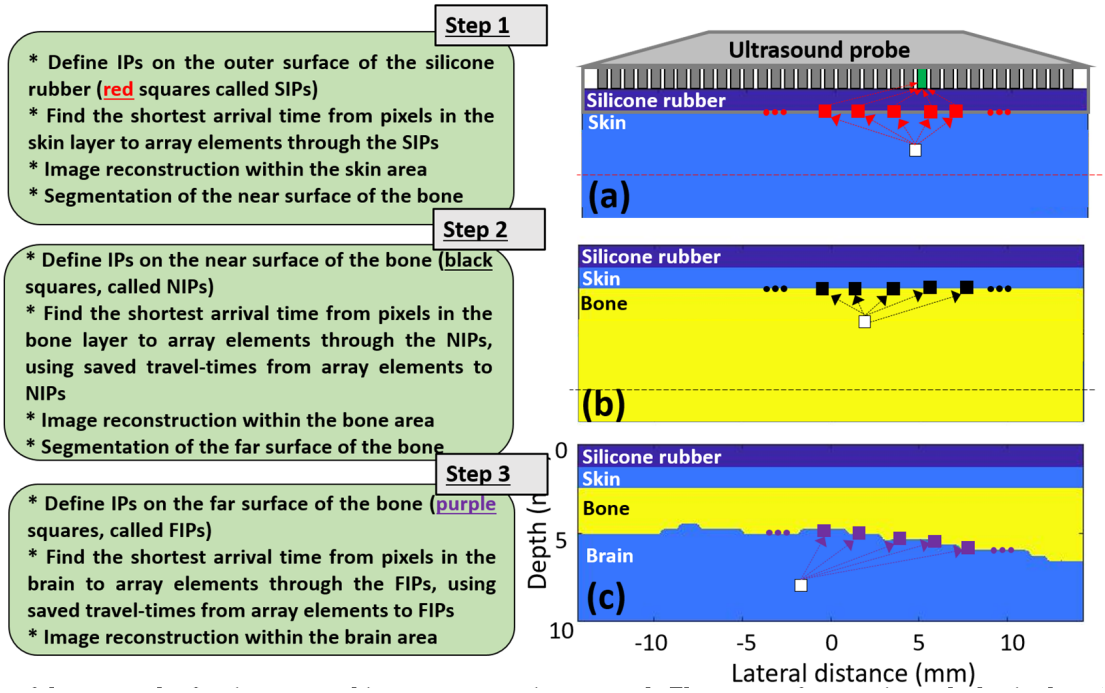

Fig. 1. (a)–(c) Summary of the proposed refraction-corrected image reconstruction approach. Three steps of ray tracing and adaptive beamforming are used for reconstructing the image in the brain area; the illustration is shown only for one pixel (white square) and one element (the element colored green). The rays pass through IPs. A limited number of IPs and travel paths are shown for simplicity. Red, black, and purple squares are IPs defined on the surface of the silicone rubber front layer in the transducer (SIPs), near (NIPs), and far (FIPs) surfaces of the bone layer, respectively. The model shown in (c) presents the numerical model used for imaging in our previous [38] and this study.

Finally, the ray tracing finds the shortest travel time from pixels in the brain (up to the maximum imaging depth) to each array element through the FIPs [the purple squares in Fig. 1(c)], and the rest of the image is reconstructed.

We use prior knowledge of the silicone rubber front layer thickness and wave speed in the silicone rubber front layer in step 1. We also assume that the wave speed in the layer between the probe and the aberrator and the wave speed in bone is known. A value from the literature [22] can be used or it can be estimated with the bidirectional head-wave technique and an autofocus approach as described in [40], [73], and [74]. Describing locally the skull as a single homogeneous layer is only valid for a temporal bone without a diploe. Moreover we hypothesize negligible wave-speed anisotropy in bone in the image plane. The depths of the first and second reconstruction steps (the red and black dashed lines, respectively, see Fig. 1) are determined by prior knowledge on the thickness of the skin and the temporal bone [20], [75]; the temporal bone thickness of the adult human skull was measured 2.5 ± 0.9 mm with CT [20]. Results obtained by the proposed reconstruction method are titled/captioned ARC (standing for Accelerated Refraction Correction technique) throughout the article. While the near surface of the bone layer is depicted flat in Fig. 1, our approach can be applied to any irregular interface (such as the far surface of the bone layer in Fig. 1).

B. GPU Implementation

1) Overview: The proposed approach for estimating the arrival times and image reconstruction are implemented in a GPU using the compute unified device architecture (CUDA) platform and the application programming interface (API) model created by Nvidia. Fig. 2 shows a schematic of the hardware/software level setup. MATLAB is used to run the Verasonics Vantage 256 system. Once the echo data of one frame are fully stored in the Vantage local memory, it is transferred to the host (PC) random access memory (RAM) using a PCI express bus; the echo data are time gain compensated and filtered (based on the bandwidth of the probe) during data acquisition by the Vantage. The echo data along with the properties of the imaging system (e.g., the properties of the array, the size of the medium, the coordinates of the pixels and primary IPs, and the minimum/maximum bone thickness) are then passed to a CUDA-written MATLAB executable (MEX) function. The MEX function synchronously and asynchronously copies the properties of the imaging system and the prebeamformed echo data to the GPU global memory, respectively, and then the image reconstruction starts.

We developed two kernels: 1) the ray-tracing kernel to find the arrival times and 2) the reconstruction kernel to form the images. These two kernels are utilized three times: 1) to find the near surface of the bone; 2) to find the far surface of the bone; and 3) to generate the final image. The travel times calculated by the ray-tracing kernel in the first two times are stored in the global memory (see the travel-time blue block in Fig. 2). This strategy makes it possible to reduce the combinational search from N_{IP}^3 (N_{IP} is the number of IPs used to describe each of the three interfaces) travel times to $3N_{\mathrm{IP}}$ for each pixel in the brain (see Fig. 1).

2) Analytic Signal Calculation: The MEX function is developed based on a sampling frequency four times of the transducer central frequency to use the direct sampling concept

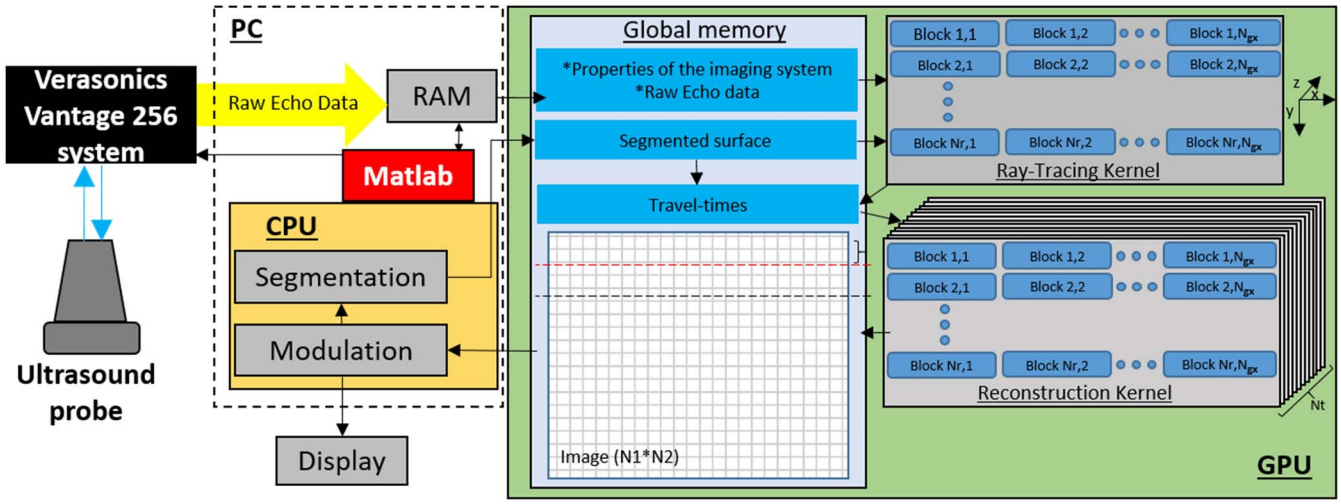

Fig. 2. System-level overview of the hardware/software setup for the GPU-based refraction-corrected image reconstruction approach. *N*gx and *N*r/*N*t are the GPU grid size in the *X*-direction and the number of receivers/transmitters, respectively. *N*1 and *N*2 are the number of image pixels in the axial and lateral directions, respectively.

[76]; the quadrature component (Q) of the analytic signal (I/Q) is approximately the in-phase signal delayed by one data sample.

3) Kernel Size: For each transmit event (Nt in total), there are Nr receivers and $N1 \times N2$ image pixels (depth $\times$ lateral direction). One-dimensional (1-D) blocks (block.x) with a size of 1024 are used in this study. The grid size used for the ray-tracing kernel is 2-D and calculated based on the number of pixels (see Section II-A), block size, and number of receivers as "dim3 grid1(N_{gx}, N_{r})"

$$N_{\mathrm{gx}} = \begin{cases} \dfrac{N_{\mathrm{OP}}}{\mathrm{block}.x}, & \dfrac{N_{\mathrm{OP}}}{\mathrm{block}.x} \in \mathbb{N} \\ \dfrac{N_{\mathrm{OP}}}{\mathrm{block}.x} + 1, & \text{else} \end{cases} \tag{1}$$

where N_{gx} and $N_{\mathrm{OP}} = N1 * N2$ are the GPU grid size in the X-direction (see Fig. 2) and the number of pixels, respectively. The GPU grid size in the Y-direction is equal to number receivers. This indicates that each row of grids calculates the correct travel times for each receiving element.

The grid used for the reconstruction kernel is 3-D. The first two dimensions are the same as the ray-tracing kernel, and the third one (in the Z-direction) is the number of transmitter (Nt).

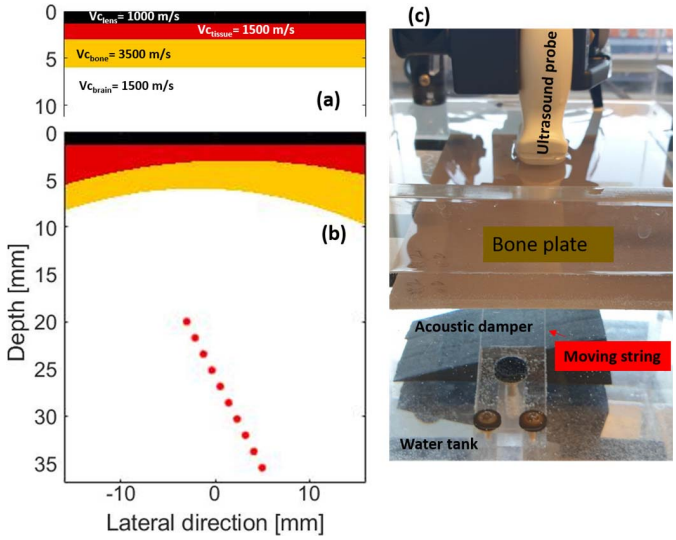

Fig. 3. Numerical models used for evaluation of the effects of pixel size on (a) accuracy of the proposed ray tracing technique to calculate travel times and (b) PSF. The red circles in (b) show the location of the scatterers. The evaluation in (a) is conducted up to a depth of 60 mm, but the model is only shown up to a depth of 12 mm for better clarity. The bone layer in (a) starts at 3 mm and ends at 6-mm depth. (c) Experimental setup with the string phantom and the bone-mimicking plate for power Doppler imaging.

III. Materials and Methods

A. Numerical and Experimental Studies

In this work, the same numerical model and experimental setups reported in [38] were used for the sake of comparison (except for evaluating the effect of pixel size on the resolution, discussed in Section II-D, and power Doppler imaging [shown in Fig. 3(b)]). For the numerical study, the k-Wave MATLAB toolbox was used in a 2-D lossless medium, and the shear wave propagation was ignored [77]. As shown in [78], neglecting mode-converted shear waves does not significantly change the main lobe of the point spread function (PSF). As a shear wave propagates slower than a compressional wave, mode-converted shear waves in bone generate additional echo signals that arrive later than those related to purely compressional waves and hence contribute only to the trailing clutter in the PSF [79]. The speed of sound in lens, skull, and soft tissue was 1000, 3200, and 1600 m/s, respectively. The mass density of the soft tissue/lens and skull was 1000 and 1900 kg/m3, respectively. A single-element transmission sequence was used to excite the medium for generating the numerical and experimental B-mode images.

A 4.2-mm-thick bone-mimicking plate (Sawbones, Pacific Research Laboratory, Inc., Vashon, WA, USA) (see Fig. 2(b) of [38]) having attenuation close to that in low-porosity cortical bone, a compressional wave speed in the image plane of 3000 m/s and mass density of 1640 kg/m^3 [41], was used in the first experiment. A sagittally cut human skull (see Fig. 2(c)

of [38]) was used in the second experiment. The temporal bone of the skull was used as the imaging window. The wave speed in the bone layer and water was considered 3500 and 1500 m/s, respectively. We imaged multiple wires having a diameter of 50 μm with a 1-D phased array probe (P4-1, ATL/Philips, 2.5 MHz, 96 elements, pitch = 0.295 mm). To reconstruct power Doppler images, a moving string was imaged with a multiangle plane wave imaging sequence (five plane waves in -15°:15° in water) with [see Fig. 3(b)] and without (to acquire a reference dataset) the Sawbones plate in front of the probe; the near surface of the Sawbones plate was at the depth of 5.7 mm. An ensemble length of 100 frames was used to compute the power Doppler images. Singular value decomposition (SVD) filtering was used to remove the stationary signals; MATLAB "svd" command was utilized and the first ten singular values were removed. Spatio-temporal SVD filtering generally performs better than a simple temporal high-pass filter for power Doppler imaging, especially when the signal-to-noise ratio is poor or with slow tissue motion [80]. The numerical and experimental images presented in the followings are reconstructed using a pixel size of 100 μm to maintain the ray tracing accuracy (discussed in Section III-C).

The PC connected to the vantage has an Intel® Xeon® E5-2680 v3 CPU and a GeForce RTX-2080Ti GPU. As our MEX function is developed based on the direct sampling concept [76], the numerical dataset obtained by a sampling frequency of 533.3 MHz was down-sampled to a sampling frequency of 10 MHz, like in the experiments, and then passed to the MEX function.

B. Evaluation Metrics

The proposed method (ARC) aims to be much faster than our previous approach relying on an Eikonal solver [fast marching technique (FMT)], while maintaining image quality. Therefore, the difference between image quality metrics assessed in ARC images and in FMT images is reported. Lateral resolution calculated as the full-width at half-maximum (FWHM) and localization error (calculated with respect to the reference images) were used for quantitative evaluation of the image quality. The axial resolution is determined by the frequency bandwidth of the transmit waveform and is not significantly degraded by phase aberration. Therefore, the axial resolution is not studied in this work.

To evaluate the effect of pixel size on the performance of the proposed ray tracing approach, the travel times were calculated for a known velocity model [see Fig. 3(a)] using an Eikonal equation solver [81] and then compared with that obtained by our method. A spatial grid step size of 5 μm was used for the Eikonal solver. The model shown in Fig. 3(b) is used to evaluate the effect of the pixel size on PSF and FWHM; ten point scatterers were positioned with lateral and axial coordinates of -3 to 5 mm and 20 to 36 mm, respectively.

The processing time of the MEX function was measured in full single-element synthetic aperture imaging (SAI) and multiangle plane (or diverging) wave imaging (PWI; with 11 virtual sources) schemes for depths of 20 mm up to 70 mm (suitable for bone imaging [40] and transcranial imaging [21], respectively) with a pixel size of 100 and 200 μm. The medium configuration shown in Fig. 3(b) was used. For each configuration, the MEX function was run 50 times and the average processing time was reported.

IV. Results

A. Numerical Results

1) Scatterers Localization and FWHM: Fig. 4(a) and (d) and Table I (the first column in the coordinates and FWHM sections) indicate that the proposed method does not significantly degrade image quality, as shown in Fig. 1(s) (see the supplementary document). The mean lateral and axial localization errors are 0 and 0.14 mm, compared with the FMT, respectively. The mean difference in lateral resolution (FWHM) is 0.04 mm, compared with FMT.

2) Effects of Pixel Size: Fig. 5(a) indicates that the pixel size does not significantly change the lateral resolution (FWHM). The PSF is not significantly altered [see Fig. 5(b)]. The maximum intensity of the PSF obtained with ARC is found very close to the true location of the scatterers indicated with the green triangle (from image without the aberrator).

Fig. 6(c) shows the absolute error calculated by subtracting the travel times obtained by the proposed ray tracing technique [see Fig. 6(a)] and the Eikonal solver [see Fig. 6(b)]; a pixel size of 200 μm was used for estimation of the travel times. The symmetry of the error map is due to symmetry of the velocity model [see Fig. 3(a)]. For pixels close to width = 0, refraction is very small such that the ray is nearly vertical because all layers are parallel to the array. Therefore, if the lateral coordinate of the pixel is equal to the lateral coordinate of the element, the error becomes extremely small; in this case, the error is minimum close to $x = 0$ for a lateral pixel coordinate of -200 μm because the lateral coordinate of the array element is -150 μm.

Fig. 6(d) shows the distribution of the errors obtained by different pixel sizes. The errors do not linearly increase with a larger pixel size since the boundaries of the velocity model at a depth of 3 and 6 mm are determined by the nearest pixel on the image grid [see Fig. 3(a)]; for a pixel size of 140 μm, it causes about 30-ns shift in the errors. Yet, the errors are below 45 ns, which is slightly larger than 10% of the ultrasound wave period (10% of 400 ns for the P4-1 probe), which results in insignificant degradation of image quality [82].

B. Experimental Results

1) Estimation of the Aberrator Thickness: Fig. 7 compares the experimental reconstructed images using the two dataset (Sawbones plate and skull) and two reconstruction methods (ARC and FMT). A thickness of 4.2 and 1.46 mm was obtained for the Sawbones plate and the temporal bone of the skull, respectively (data not shown here). The thickness of the Sawbones plate is in excellent agreement with that obtained with the FMT [38]. The skull thickness is about 0.16 mm larger with the ARC technique compared with the FMT [38]; this error is considered minor comparing with the pixel size of 100 μm. The image quality in Fig. 7(a) and (c) is close to

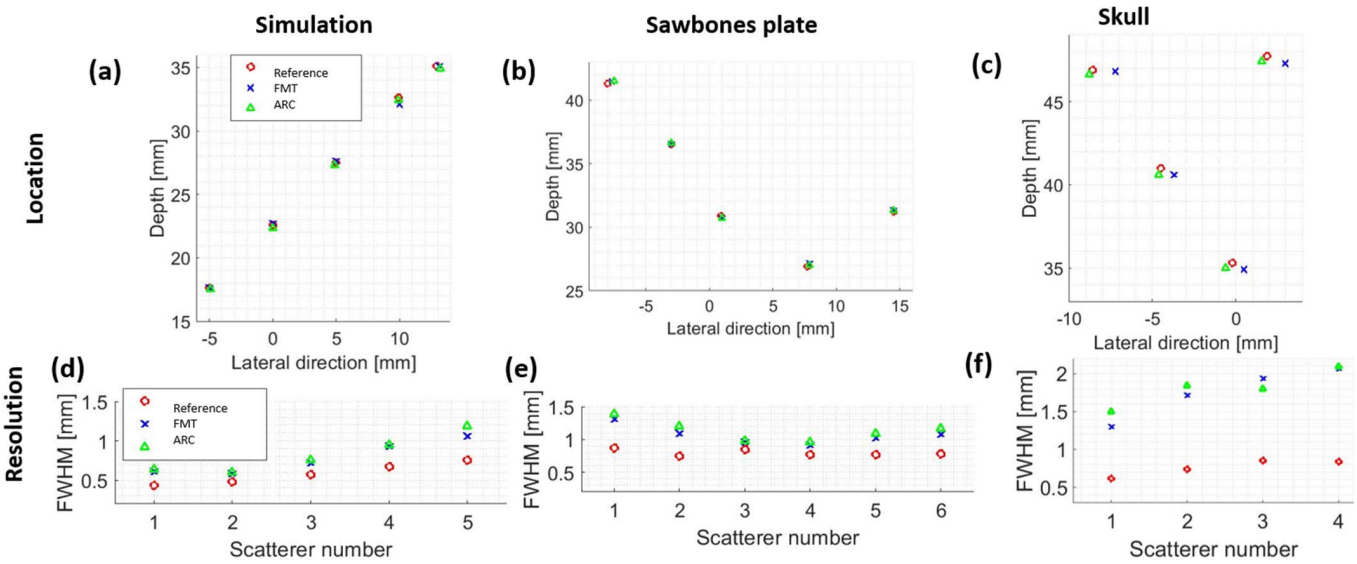

Fig. 4. (a), (d) Scatterers' coordinates and FWHM obtained in the simulation study (the first column), and the experiments conducted with the (b), (e) Sawbones plate (the second column) and the (c), (f) skull (the third column). The detailed numbers corresponding to the reference and FMT can be found in Tables I–III of the supplementary document of [38]. The reference image was generated without an aberrator in front of the probe.

TABLE I

QUANTITATIVE EVALUATION OF IMAGE QUALITY OBTAINED WITH THE ARC TECHNIQUE COMPARED WITH OUR PREVIOUS APPROACH RELYING ON AN EIKONAL SOLVER FOR THE NUMERICAL AND EXPERIMENTAL RESULTS PRESENTED IN FIGS. 4 AND 5. THE LOCALIZATION ERROR AND LATERAL FWHM DIFFERENCE WERE CALCULATED WITH RESPECT TO THE EIKONAL SOLVER APPROACH RELYING ON AN FMT; SEE TABLES I–III OF THE SUPPLEMENTARY DOCUMENT OF [38]

Scatterer number	Localization error (mm) [Lateral, Axial]			Lateral FWHM difference (mm)		
	Simulation	Sawbones plate	Skull	Simulation	Sawbones plate	Skull
1	[0.1, -0.1]	[0, 0]	[-1.1, 0.1]	0.0	0.08	0.2
2	[0, -0.4]	[0.2, 0]	[-0.9, 0]	0.02	0.11	0.13
3	[-0.1, -0.3]	[0, 0.1]	[-1.6, -0.2]	0.03	0.03	-0.13
4	[-0.1, 0.3]	[0, 0]	[-1.44, 0.1]	0.02	0.04	0.03
5	[0.1, -0.2]	[0, -0.1]	---	0.13	0.07	---
6	---	[0, 0]	---	---	0.09	---
	Mean ± standard deviation			**Mean ± standard deviation**		
	[0±0.1, 0.14±0.27]	[0.03±0.08, 0±0.06]	[-1.2±0.31, 0±0.14]	0.04±0.05	0.07±0.03	0.05±0.14

Fig. 7(b) and (d), which is our goal. The red boxes show the effects of multiple scattering caused by the aberrator.

2) Scatterers Localization and FWHM (Sawbones Plate): Fig. 4(b) and (e) and Table I (the second column in the coordinates and FWHM sections) indicate that the proposed method reconstructs the scatterers with an average lateral and axial localization error of 0.03 and 0 mm, compared with FMT, respectively. The mean difference in lateral resolution (FWHM) is 0.07 mm, compared with FMT.

3) Scatterers Localization and FWHM (Human Skull): Fig. 4(c) and (f) and Table I (the third column in the coordinates and FWHM sections) indicate that the proposed method reconstructs the scatterers with an average lateral and axial localization error of −1.2 and 0 mm, compared with the FMT, respectively. The lateral error is 0.3 mm with respect

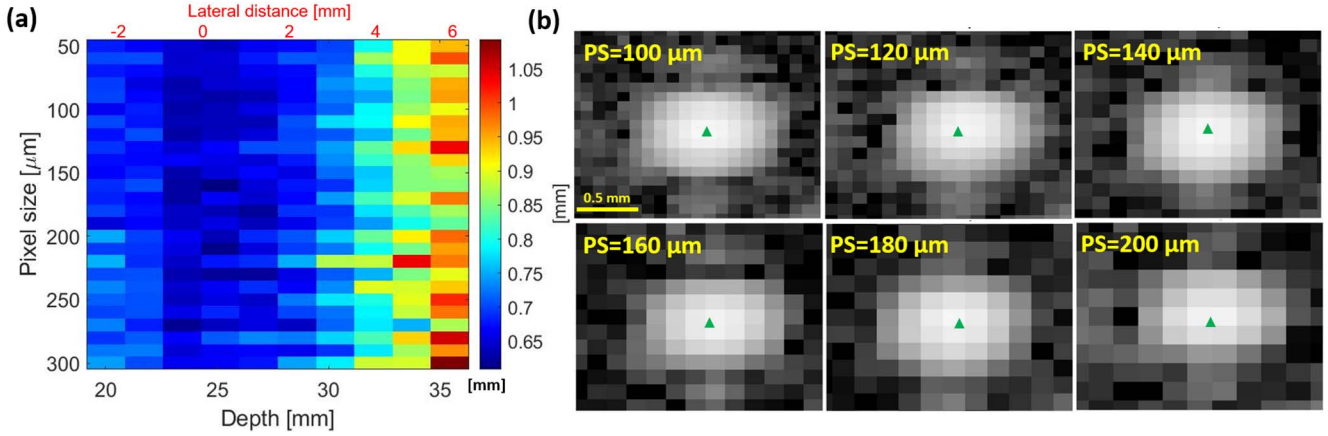

Fig. 5. (a) Lateral FWHM (see the colorbar for the scale) at different axial (depth) and lateral locations and for different pixel sizes, obtained with the numerical model shown in Fig. 3(b); the black and red *x*-axes show the depth and the lateral locations of the scatterers positioned obliquely, respectively. (b) PSF obtained for different pixel sizes; the scatterer was positioned at the lateral and axial distance of −3 and 20 mm, respectively. The green mark indicates the true location of the scatterer. The PSFs are shown with a dynamic range of 40 dB. PS stands for the pixel size.

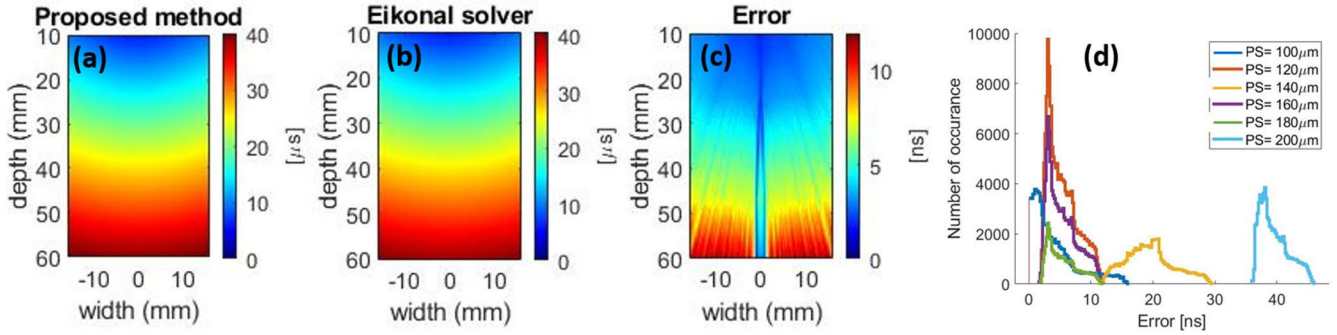

Fig. 6. Travel times between the center element of the transducer array and pixels in the brain estimated with (a) proposed ray tracing ARC technique for a pixel size of 200 μm and (b) accurate travel times calculated with an Eikonal solver, respectively, using the configuration shown in Fig. 3(a). (c) Absolute error map (which is obtained by subtracting (a) and (b). (d) Distribution of the errors on the travel times from an element in the center of the transducer aperture to pixels in the brain, for different pixel sizes. PS stands for the pixel size.

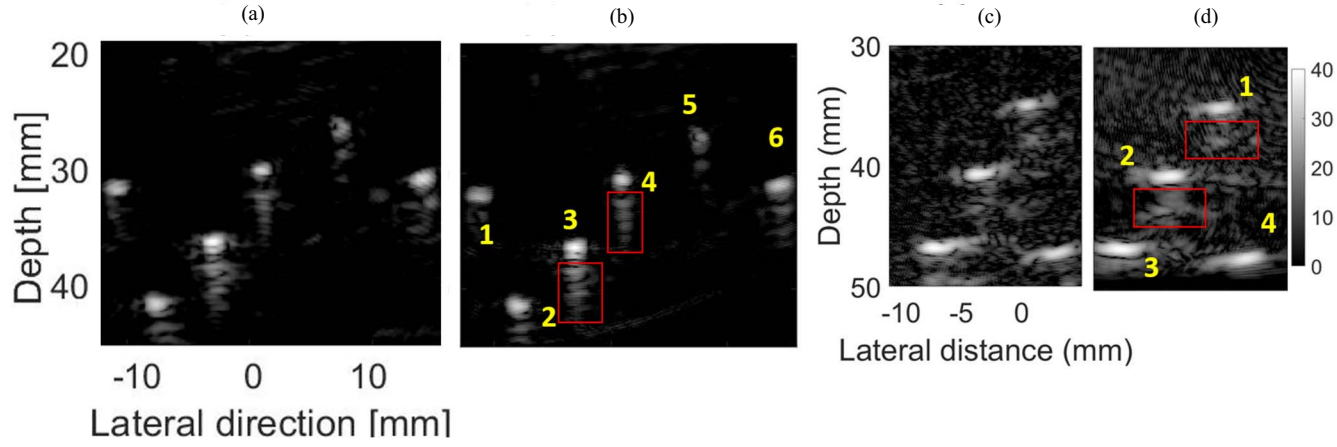

Fig. 7. Experimental reconstructed image with (a) and (b) sawbones plate and (c) and (d) real human skull in front of the probe. All the images are locally normalized and log-compressed. The red boxes show the effects of multiple scattering caused by the aberrating layer (plate and bone). The numbers (in yellow) are referred for quantitative evaluation in Table I and Fig. 4.

to reference image (values are available in the supplementary document of [38]) though. The mean difference in lateral resolution (FWHM) is 0.05 mm, compared with FMT.

4) Power Doppler Imaging: The reconstructed power Doppler images with or without the Sawbones plate in front of the probe are presented in Fig. 8. The yellow arrows in Fig. 8(a) show bubbles floating in the water tank. With the aberrator inserted, the clutter around the string is significantly weaker in the image reconstructed by the ARC technique, compared with the conventional reconstruction which ignores the aberrator. The width of string (measured as the FWHM in a direction normal to the string) was 0.37 mm with the ARC technique [see Fig. 8(c)], which is close to the width in the reference image (0.32 mm). The width of the wire obtained

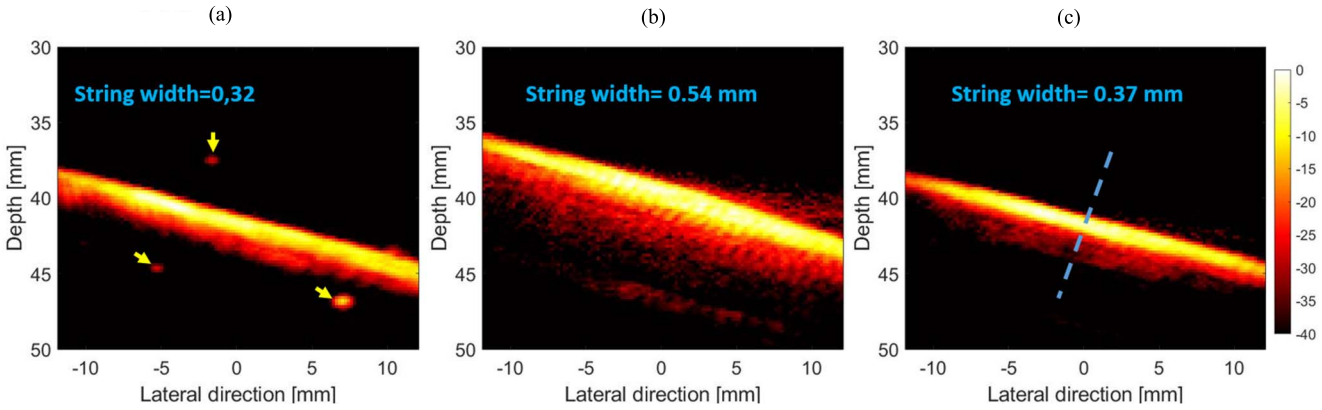

Fig. 8. Power Doppler images using the experimental dataset generated (a) without and (b) and (c) with the Sawbones plate in front of the probe [see Fig. 3(c)]. The yellow arrows in (a) show bubbles floating in the water tank. The blue dashed line shows the line (normal to the string) used to calculate the width of the string. The reference image was generated without an aberrator in front of the probe.

TABLE II
PROCESSING TIME OF EACH STEP OF THE ARC TECHNIQUE FOR PWI WITH 11 TRANSMIT STEERED PLANE WAVES AND AN IMAGE DEPTH OF 70 MM

Processing modules	Time [ms]
Primary memory allocation	8
First layer ray-tracing	6
First layer reconstruction	1
Second layer ray-tracing	5
Second layer reconstruction	1
Third layer ray-tracing	6
Third layer reconstruction	2
memory allocation and deallocation, segmentation	2
Total	31

with conventional reconstruction appears wider (0.54 mm) as a consequence of degraded lateral resolution caused by phase aberration.

C. Processing Time With the GPU Implementation of the ARC Technique

The processing time of the proposed reconstruction approach, calculated for the configuration shown in Fig. 3(b), is presented in Fig. 9. The red and black curves represent the processing time and frame rate, respectively. The frame rate with a pixel size of 100 μm is lower than with a pixel size of 200 μm, because the processing time increases with the number of pixels. Using SAI scheme with 96 single-element transmissions to reconstruct the image up to depths of 20 and 70 mm, a frame rate of 32 and 19 Hz is obtained for a pixel size of 200 μm. Using PWI scheme with 11 transmit steered plane waves to reconstruct the image up to depths of 20 and 70 mm, a frame rate of 40 and 32 Hz is obtained for a pixel size of 200 μm. The processing time for each step in the ARC technique for PWI mode and an imaging depth of 70 mm with a pixel size of 200 μm is presented in Table II.

V. DISCUSSION

A. Imaging Scheme

To calculate the round-trip travel times that are required to reconstruct the image with a delay-and-sum algorithm, both the transmit and receive travel times are needed. In full single-element SAI scheme, the number of transmitters (Nt) and receivers (Nr) and their coordinates are the same. Therefore, the receive travel times calculated with respect to Nr receivers (see the ray-tracing kernel in Fig. 2) can be used as transmit travel times. In practice, however, single-element SAI is likely not the optimal imaging strategy for TUI due to: 1) a low signal-to-noise ratio (i.e., transmitting with a single element generates a low acoustic pressure in the brain) and 2) a low data acquisition frame rate, which does not allow blood flow quantification in the brain (usually used for diagnosis of brain disorders) [83]. To address these issues, PWI [84] and diverging waves imaging (DWI) [85] schemes have a great potential since: 1) a good image quality can be achieved while a faster data acquisition allows capturing transient phenomena in the brain, as reported by Montaldo *et al.* [86]; and 2) transmitting with subapertures or with all the elements of the probe (with appropriate transmit delays) ensures a good signal-to-noise ratio. For TUI with a phased array transducer, DWI is more desired as it enables a larger field of view, compared with PWI. Using PWI/ DWI schemes requires estimating the transmit travel times from virtual transmitters (usually defined behind the ultrasound probe) to pixels. This requires an additional ray tracing in steps 2, 4, and 6 of Section II-A. To do so, the ray-tracing kernel in Fig. 2 is configured with a Z grid size equal to the number of virtual transmitters.

As presented in Fig. 9, PWI or DWI offers faster image reconstruction compared with single-element SAI. That is because: 1) the size of the third dimension (Z) of the reconstruction kernel (see Fig. 2) equals to the number of virtual transmitter (from 3 [87] to 15 [88]); 2) less load/copy transactions from the global memory to on-chip memories, and the other way around, are needed; and 3) the additional ray tracing (for estimating the transmit travel times) is not computationally expensive. It should be noted that the processing time for PWI and DWI with the same number of virtual transmitters is the same.

B. Analytic Signal Calculation

Yiu *et al.* [70] and Gonzalez and Bell [55] used Hilbert transform in the time and frequency domain to calculate the analytic echo data, respectively. In this study, however, the

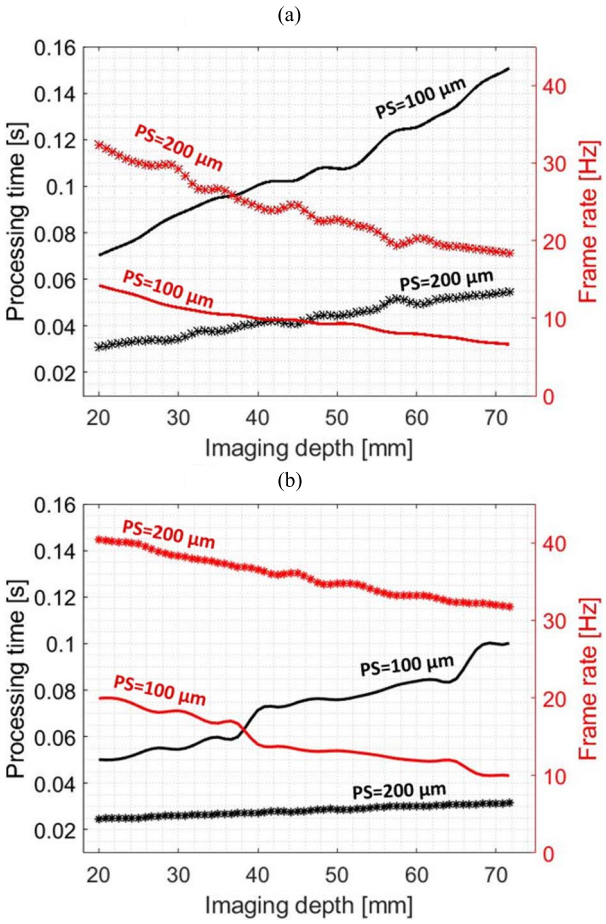

Fig. 9. Processing time/frame rate of the MEX function in (a) full single-element SAI and (b) plane wave imaging/DWI (with 11 steering angles) schemes for different imaging depths and pixel sizes (PS). The black and red graphs belong to the left (processing time) and right (frame rate) horizontal panels, respectively.

direct sampling concept is used to avoid dedicating processing power to calculate the analytic signal, which includes copy/load memory transactions as well [76]. The same methodology was used by Choe *et al.* [62] before.

C. Limitations of the Proposed Approach

1) Wave-Speed Modeling: While the cortical bone of the temporal region of the skull is known to exhibit anisotropic wave speed [22], the wave speed in the bone layer was assumed isotropic to simplify ray tracing and, therefore, enable the fastest frame rate with our approach. Image distortions (depending on the anisotropy level) are expected if the anisotropy is neglected.

2) Implementation: As can be seen in Table II, there are two modules that increase the processing time: 1) primary memory allocation and 2) ray-tracing kernel.

a) Memory allocation: The primary memory allocation includes defining host (CPU) memories to save the results of the GPU kernels/CPU functions and copying the properties of the imaging system to the GPU global memory (as shown in Fig. 2). Currently, the memory allocation, and also memory freeing at the end of the MEX function, happens each time the MEX function runs. To further increase the frame rate, MATLAB GPU arrays can be used to define these memories once (when the MEX function runs for the first time), and free them at the end of imaging. It should be also mentioned that the RF-data are transferred to the global memory in an asynchronous way during the first reconstruction step. Therefore, the size of the RF-data is not a bottleneck.

b) Ray-tracing kernel: Our ray-tracing kernel calculates the travel time of all the pixels in parallel. However, finding the shortest travel time between a pixel and an array element through IPs is implemented sequentially with a for-loop in GPU. This kernel can be improved by re-defining the kernel architecture in a way that it evaluates all the travel times (through the IPs) in parallel. Another option is to implement it on CPU with parallel programming (such an OpenMP). In the current implementation, ray tracing is calculated for each frame because the position and geometry of the skull (in the current image plane) must be updated to achieve real-time refraction-corrected TUI as the sonographer moves the probe to search for the optimal image plane. However, once the proper imaging window and imaging plane are found by the operator and the probe is stabilized on the temporal bone, the travel times could be only calculated once and reused as long as the probe remains still. An automated approach could be implemented to evaluate the stability of the probe in order to decide whether or not the refraction-corrected travel times must be updated. This would further increase the frame rate of our method.

D. Future Work

Our future studies include the *in vivo* evaluation of the proposed approach in adult human subjects, the development of a GPU-accelerated reconstruction technique that addresses the wave speed anisotropy in the bone layer and the bottlenecks discussed in Section IV-C2, and the translation of the approach to a matrix array transducer where the 3-D geometry of the skull will be described.

VI. Conclusion

In this article, we reported a reconstruction technique for TUI through the temporal bone, which uses a fast ray-tracing approach and a GPU implementation to speed up the calculation of the refraction-corrected arrival times and image reconstruction. The results showed that the error on travel times using a pixel size of 200 μm is not significant (about 10% of the ultrasound temporal period at 2.5 MHz), and hence resulting in insignificant degradation of image quality and resolution, and negligible localization errors. We believe the approach enables real-time refraction-corrected TUI with a frame rate between 20 and 30 Hz, and real-time refraction-corrected power Doppler imaging.

References

[1] J. C. Somer, "The history of real time ultrasound," *Int. Congr. Ser.*, vol. 1274, pp. 3–13, Oct. 2004.
[2] F. J. Fry and J. E. Barger, "Acoustical properties of the human skull," *J. Acoust. Soc. Amer.*, vol. 63, pp. 1576–1590, May 1978.
[3] F. Vignon, J.-F. Aubry, M. Tanter, A. Margoum, and M. Fink, "Adaptive focusing for transcranial ultrasound imaging using dual arrays," *J. Acoust. Soc. Amer.*, vol. 120, no. 5, pp. 2737–2745, Aug. 2015.

[4] G. Pinton, J.-F. Aubry, E. Bossy, M. Müller, M. Pernot, and M. Tanter, "Attenuation, scattering, and absorption of ultrasound in the skull bone," *Med. Phys.*, vol. 39, pp. 299–307, Jan. 2012.

[5] L. Saba and E. Raz, *Neurovascular Imaging: From Basics to Advanced Concepts*. Berlin, Germany: Springer, 2016.

[6] V. I. Lau *et al.*, "Better with ultrasound: Transcranial Doppler," *Chest*, vol. 157, no. 1, pp. 142–150, 2020.

[7] J. D. Kirsch, M. Mathur, M. H. Johnson, G. Gowthaman, and L. M. Scoutt, "Advances in transcranial Doppler U.S.: Imaging ahead," *RadioGraphics*, vol. 33, no. 1, pp. 1–14, Jan. 2013.

[8] H. White and B. Venkatesh, "Applications of transcranial Doppler in the ICU: A review," *Intensive Care Med.*, vol. 32, no. 7, pp. 981–994, 2006.

[9] T. Hölscher *et al.*, "Transcranial ultrasound from diagnosis to early stroke treatment," *Cerebrovascular Diseases*, vol. 26, no. 6, pp. 659–663, 2008.

[10] F. Schlachetzki *et al.*, "Transcranial ultrasound from diagnosis to early stroke treatment—Part 2: Prehospital neurosonography in patients with acute stroke—The regensburg stroke mobile project," *Cerebrovascular Diseases*, vol. 33, no. 3, pp. 262–271, 2012.

[11] T. Holscher, "Prehospital use of portable ultrasound for stroke diagnosis and treatment initiation," *Air Rescue*, vol. 2, pp. 48–50, Feb. 2012.

[12] D. Antipova, L. Eadie, S. Makin, H. Shannon, P. Wilson, and A. Macaden, "The use of transcranial ultrasound and clinical assessment to diagnose ischaemic stroke due to large vessel occlusion in remote and rural areas," *PLoS ONE*, vol. 15, no. 10, Oct. 2020, Art. no. e0239653.

[13] M. Herzberg *et al.*, "Prehospital stroke diagnostics based on neurological examination and transcranial ultrasound," *Crit. Ultrasound J.*, vol. 6, no. 1, pp. 1–13, Dec. 2014.

[14] R. J. Adams, "TCD in sickle cell disease: An important and useful test," *Pediatric Radiol.*, vol. 35, no. 3, pp. 229–234, Mar. 2005.

[15] R. J. Adams and D. Brambilla, "Discontinuing prophylactic transfusions used to prevent stroke in sickle cell disease," *New England J. Med.*, vol. 353, no. 26, pp. 2769–2778, 2005.

[16] R. J. Adams *et al.*, "Prevention of a first stroke by transfusions in children with sickle cell anemia and abnormal results on transcranial Doppler ultrasonography," *New England J. Med.*, vol. 339, no. 1, pp. 5–11, Jul. 1998.

[17] R. J. Adams, F. T. Nichols, R. Figueroa, V. McKie, and T. Lott, "Transcranial Doppler correlation with cerebral angiography in sickle cell disease," *Stroke*, vol. 23, no. 8, pp. 1073–1077, Aug. 1992.

[18] D. W. Newell, S. M. Grady, J. M. Eskridge, and R. H. Winn, "Distribution of angiographic vasospasm after subarachnoid hemorrhage: Implications for diagnosis by transcranial Doppler ultrasonography," *Neurosurgery*, vol. 27, no. 4, pp. 574–577, Oct. 1990.

[19] Y. Y. Vora, M. Suarez-Almazor, D. E. Steinke, M. L. Martin, and J. M. Findlay, "Role of transcranial Doppler monitoring in the diagnosis of cerebral vasospasm after subarachnoid hemorrhage," *Neurosurgery*, vol. 44, no. 6, pp. 1237–1248, Jun. 1999.

[20] R. T. Brisson *et al.*, "Association between tomographic characteristics of the temporal bone and transtemporal window quality on transcranial color Doppler ultrasound in patients with stroke or transient ischemic attack," *Ultrasound Med. Biol.*, vol. 47, no. 3, pp. 511–516, Mar. 2021.

[21] C.-H. Lee, S.-H. Jeon, S.-J. Wang, B.-S. Shin, and H. G. Kang, "Factors associated with temporal window failure in transcranial Doppler sonography," *NeuroLog. Sci.*, vol. 41, no. 11, pp. 3293–3299, Nov. 2020.

[22] J. Peterson and P. C. Dechow, "Material properties of the human cranial vault and zygoma," *Anatomical Rec. A, Discoveries Mol., Cellular, Evol. Biol., Off. Publication Amer. Assoc. Anatomists*, vol. 274, no. 1, pp. 785–797, Sep. 2003.

[23] J.-H. Kwon, J. S. Kim, D.-W. Kang, K.-S. Bae, and S. U. Kwon, "The thickness and texture of temporal bone in brain CT predict acoustic window failure of transcranial Doppler," *J. Neuroimag.*, vol. 16, no. 4, pp. 347–352, Oct. 2006.

[24] S. Baykov *et al.*, "Physical and technical aspects of ultrasonic brain imaging through thick skull bones: 2. Experimental studies," *Acoust. Phys.*, vol. 49, no. 4, pp. 389–395, Jul. 2003.

[25] S. V. Baikov, A. M. Molotilov, and V. D. Svet, "Physical and technological aspects of ultrasonic imaging of brain structures through thick skull bones: 1. Theoretical and model studies," *Acoust. Phys.*, vol. 49, no. 3, pp. 276–284, May 2003.

[26] J. J. Dahl, M. S. Soo, and G. E. Trahey, "Spatial and temporal aberrator stability for real-time adaptive imaging," *IEEE Trans. Ultrason., Ferroelectr., Freq. Control*, vol. 52, no. 9, pp. 1504–1517, Sep. 2005.

[27] F. Vignon, J.-F. Aubry, M. Tanter, A. Margoum, M. Fink, and J. Lecoeur, "Dual-arrays brain imaging prototype: Experimental *in vitro* results," in *Proc. IEEE Int. Ultrason. Symp.*, Sep. 2005, pp. 504–507.

[28] N. M. Ivancevich, J. J. Dahl, G. E. Trahey, and S. W. Smith, "Phase-aberration correction with a 3-D ultrasound scanner: Feasibility study," *IEEE Trans. Ultrason., Ferroelectr., Freq. Control*, vol. 53, no. 8, pp. 1432–1439, Aug. 2006.

[29] N. M. Ivancevich, G. F. Pinton, H. A. Nicoletto, E. Bennett, D. T. Laskowitz, and S. W. Smith, "Real-time 3-D contrast-enhanced transcranial ultrasound and aberration correction," *Ultrasound Med. Biol.*, vol. 34, no. 9, pp. 1387–1395, Sep. 2008.

[30] N. M. Ivancevich, J. J. Dahl, and S. W. Smith, "Comparison of 3-D multi-lag cross-correlation and speckle brightness aberration correction algorithms on static and moving targets," *IEEE Trans. Ultrason., Ferroelectr., Freq. Control*, vol. 56, no. 10, pp. 2157–2166, Oct. 2009.

[31] T. Wang and Y. Jing, "Transcranial ultrasound imaging with speed of sound-based phase correction: A numerical study," *Phys. Med. Biol.*, vol. 58, no. 19, p. 6663, 2013.

[32] X. Lin, M. Sun, Y. Liu, Z. Shen, Y. Shen, and N. Feng, "Variable speed of sound compensation in the linear-array photoacoustic tomography using a multi-stencils fast marching method," *Biomed. Signal Process. Control*, vol. 44, pp. 67–74, Jul. 2018.

[33] K. Shapoori, J. Sadler, A. Wydra, E. V. Malyarenko, A. N. Sinclair, and R. G. Maev, "An ultrasonic-adaptive beamforming method and its application for trans-skull imaging of certain types of head injuries; Part I: Transmission mode," *IEEE Trans. Biomed. Eng.*, vol. 62, no. 5, pp. 1253–1264, May 2015.

[34] C. Jiang *et al.*, "Ray theory-based transcranial phase correction for intracranial imaging: A phantom study," *IEEE Access*, vol. 7, pp. 163013–163021, 2019.

[35] Y. Jing, F. C. Meral, and G. T. Clement, "Time-reversal transcranial ultrasound beam focusing using a k-space method," *Phys. Med. Biol.*, vol. 57, no. 4, p. 901, 2012.

[36] G. Bouchoux *et al.*, "Experimental validation of a finite-difference model for the prediction of transcranial ultrasound fields based on CT images," *Phys. Med. Biol.*, vol. 57, no. 23, p. 8005, 2012.

[37] C. Jiang, Y. Li, K. Xu, and D. Ta, "Full-matrix phase shift migration method for transcranial ultrasonic imaging," *IEEE Trans. Ultrason., Ferroelectr., Freq. Control*, vol. 68, no. 1, pp. 72–83, Jan. 2021.

[38] M. Mozaffarzadeh, E. Verschuur, M. D. Verweij, V. Daeichin, N. De Jong, and G. Renaud, "Refraction-corrected transcranial ultrasound imaging through the human temporal window using a single probe," *IEEE Trans. Ultrason., Ferroelectr., Freq. Control*, vol. 69, no. 4, pp. 1191–1203, Apr. 2022.

[39] J. Shepherd, G. Renaud, P. Clouzet, and K. van Wijk, "Photoacoustic imaging through a cortical bone replica with anisotropic elasticity," *Appl. Phys. Lett.*, vol. 116, no. 24, Jun. 2020, Art. no. 243704.

[40] G. Renaud, P. Kruizinga, D. Cassereau, and P. Laugier, "*In vivo* ultrasound imaging of the bone cortex," *Phys. Med. Biol.*, vol. 63, no. 12, Jun. 2018, Art. no. 125010.

[41] G. Renaud, P. Clouzet, D. Cassereau, and M. Talmant, "Measuring anisotropy of elastic wave velocity with ultrasound imaging and an autofocus method: Application to cortical bone," *Phys. Med. Biol.*, vol. 65, no. 23, Dec. 2020, Art. no. 235016.

[42] J. A. Sethian, *Level Set Methods and Fast Marching Methods: Evolving Interfaces in Computational Geometry, Fluid Mechanics, Computer Vision, and Materials Science*. Cambridge, U.K.: Cambridge Univ. Press, 1999.

[43] M. S. Hassouna and A. A. Farag, "Multistencils fast marching methods: A highly accurate solution to the Eikonal equation on Cartesian domains," *IEEE Trans. Pattern Anal. Mach. Intell.*, vol. 29, no. 9, pp. 1563–1574, Sep. 2007.

[44] D. A. Waltham, "Two-point ray tracing using fermat's principle," *Geophys. J. Int.*, vol. 93, no. 3, pp. 575–582, Jun. 1988.

[45] S. R. M. Rostami and M. Ghaffari-Miab, "Finite difference generated transient potentials of open-layered media by parallel computing using OpenMP, MPI, OpenACC, and CUDA," *IEEE Trans. Antennas Propag.*, vol. 67, no. 10, pp. 6541–6550, Oct. 2019.

[46] K. Oh and K. Jung, "GPU implementation of neural networks," *Pattern Recognit.*, vol. 37, pp. 1311–1314, Jun. 2004.

[47] J. Krüger and R. Westermann, "Linear algebra operators for GPU implementation of numerical algorithms," *ACM SIGGRAPH Courses*, p. 234, Jul. 2005.

[48] H. K.-H. So, J. Chen, B. Y. S. Yiu, and A. C. H. Yu, "Medical ultrasound imaging: To GPU or not to GPU?" *IEEE Micro*, vol. 31, no. 5, pp. 54–65, Sep./Oct. 2011.

[49] J. Chen, B. Y. S. Yiu, H. K.-H. So, and A. C. H. Yu, "Real-time GPU-based adaptive beamformer for high quality ultrasound imaging," in *Proc. IEEE Int. Ultrason. Symp.*, Oct. 2011, pp. 474–477.
[50] D. Hyun, G. E. Trahey, and J. J. Dahl, "*In vivo* demonstration of a real-time simultaneous B-mode/spatial coherence GPU-based beamformer," in *Proc. IEEE Int. Ultrason. Symp. (IUS)*, Jul. 2013, pp. 1280–1283.
[51] J. Chen, B. Y. S. Yiu, B. K. Hamilton, A. C. H. Yu, and H. K.-H. So, "Design space exploration of adaptive beamforming acceleration for bedside and portable medical ultrasound imaging," *ACM SIGARCH Comput. Archit. News*, vol. 39, no. 4, pp. 20–25, Sep. 2011.
[52] J. P. Åsen, J. I. Buskenes, C.-I. C. Nilsen, A. Austeng, and S. Holm, "Implementing Capon beamforming on a GPU for real-time cardiac ultrasound imaging," *IEEE Trans. Ultrason., Ferroelectr., Freq. Control*, vol. 61, no. 1, pp. 76–85, Jan. 2014.
[53] B. Y. S. Yiu and A. C. H. Yu, "GPU-based minimum variance beamformer for synthetic aperture imaging of the eye," *Ultrasound Med. Biol.*, vol. 41, no. 3, pp. 871–883, Mar. 2015.
[54] D. Hyun, G. E. Trahey, and J. Dahl, "A GPU-based real-time spatial coherence imaging system," in *Proc. SPIE*, vol. 8675, Mar. 2013, Art. no. 86751B.
[55] E. A. Gonzalez and M. A. L. Bell, "GPU implementation of photoacoustic short-lag spatial coherence imaging for improved image-guided interventions," *J. Biomed. Opt.*, vol. 25, no. 7, 2020, Art. no. 077002.
[56] E. Gonzalez, M. R. Gubbi, and M. A. L. Bell, "GPU implementation of coherence-based photoacoustic beamforming for autonomous visual servoing," in *Proc. IEEE Int. Ultrason. Symp. (IUS)*, Oct. 2019, pp. 24–27.
[57] T. Kjeldsen *et al.*, "Synthetic aperture sequential beamforming implemented on multi-core platforms," in *Proc. IEEE Int. Ultrason. Symp.*, Sep. 2014, pp. 2181–2184.
[58] M. C. Hemmsen *et al.*, "Implementation of synthetic aperture imaging on a hand-held device," in *Proc. IEEE Int. Ultrason. Symp.*, Sep. 2014, pp. 2177–2180.
[59] S. Jeon, E.-Y. Park, W. Choi, R. Managuli, K. J. Lee, and C. Kim, "Real-time delay-multiply-and-sum beamforming with coherence factor for *in vivo* clinical photoacoustic imaging of humans," *Photoacoustics*, vol. 15, Sep. 2019, Art. no. 100136.
[60] S. R. M. Rostami, M. Mozaffarzadeh, M. Ghaffari-Miab, A. Hariri, and J. Jokerst, "GPU-accelerated double-stage delay-multiply-and-sum algorithm for fast photoacoustic tomography using LED excitation and linear arrays," *Ultrason. Imag.*, vol. 41, no. 5, pp. 301–316, Sep. 2019.
[61] M. Mozaffarzadeh, A. Mahloojifar, M. Orooji, S. Adabi, and M. Nasiriavanaki, "Double-stage delay multiply and sum beamforming algorithm: Application to linear-array photoacoustic imaging," *IEEE Trans. Biomed. Eng.*, vol. 65, no. 1, pp. 31–42, Jan. 2018.
[62] J. W. Choe, A. Nikoozadeh, O. Oralkan, and B. T. Khuri-Yakub, "GPU-based real-time volumetric ultrasound image reconstruction for a ring array," *IEEE Trans. Med. Imag.*, vol. 32, no. 7, pp. 1258–1264, Jul. 2013.
[63] J. Zhou *et al.*, "Low complexity 3D ultrasound imaging using synthetic aperture sequential beamforming," in *Proc. IEEE Int. Workshop Signal Process. Syst. (SiPS)*, Oct. 2016, pp. 33–38.
[64] M. B. Stuart *et al.*, "Real-time volumetric synthetic aperture software beamforming of row–column probe data," *IEEE Trans. Ultrason., Ferroelectr., Freq. Control*, vol. 68, no. 8, pp. 2608–2618, Aug. 2021.
[65] D. Hyun, Y. L. Li, I. Steinberg, M. Jakovljevic, T. Klap, and J. J. Dahl, "An open source GPU-based beamformer for real-time ultrasound imaging and applications," in *Proc. IEEE Int. Ultrason. Symp. (IUS)*, Oct. 2019, pp. 20–23.
[66] J. W. Choe, A. Nikoozadeh, O. Oralkan, and B. T. Khuri-Yakub, "GPU-based real-time imaging software suite for medical ultrasound," in *Proc. IEEE Int. Ultrason. Symp. (IUS)*, Jul. 2013, pp. 2057–2060.
[67] Y. Du, Y. Shen, B. Y. S. Yiu, A. C. H. Yu, and L. Zhu, "High frame rate vector flow imaging: Development as a new diagnostic mode on a clinical scanner," in *Proc. IEEE Int. Ultrason. Symp. (IUS)*, Oct. 2018, pp. 1–4.
[68] J. A. Ketterling *et al.*, "High-speed, high-frequency ultrasound, in utero vector-flow imaging of mouse embryos," *Sci. Rep.*, vol. 7, no. 1, pp. 1–9, Dec. 2017.
[69] B. Y. S. Yiu, S. S. M. Lai, and A. C. H. Yu, "Vector projectile imaging: Time-resolved dynamic visualization of complex flow patterns," *Ultrasound Med. Biol.*, vol. 40, no. 9, pp. 2295–2309, Sep. 2014.
[70] B. Y. S. Yiu, I. K. H. Tsang, and A. C. H. Yu, "GPU-based beamformer: Fast realization of plane wave compounding and synthetic aperture imaging," *IEEE Trans. Ultrason., Ferroelectr., Freq. Control*, vol. 58, no. 8, pp. 1698–1705, Aug. 2011.
[71] T. Moser, "Shortest path calculation of seismic rays," *Geophysics*, vol. 56, no. 1, pp. 59–67, Jan. 1991.
[72] D. Hong, "Medical image segmentation based on accelerated Dijkstra algorithm," in *Advances in Intelligent Systems* (Advances in Intelligent and Soft Computing). Berlin, Germany: Springer, 2012, pp. 341–348.
[73] M. Mozaffarzadeh, C. Minonzio, N. de Jong, M. D. Verweij, S. Hemm, and V. Daeichin, "Lamb waves and adaptive beamforming for aberration correction in medical ultrasound imaging," *IEEE Trans. Ultrason., Ferroelectr., Freq. Control*, vol. 68, no. 1, pp. 84–91, Jan. 2021.
[74] M. Mozaffarzadeh *et al.*, "Erratum to 'Lamb waves and adaptive beamforming for aberration correction in medical ultrasound imaging,'" *IEEE Trans. Ultrason., Ferroelectr., Freq. Control*, vol. 68, no. 2, pp. 352–353, Feb. 2021.
[75] W. Qiu, A. Bouakaz, E. E. Konofagou, and H. Zheng, "Ultrasound for the brain: A review of physical and engineering principles, and clinical applications," *IEEE Trans. Ultrason., Ferroelectr., Freq. Control*, vol. 68, no. 1, pp. 6–20, Jan. 2021.
[76] K. Ranganathan, M. K. Santy, T. N. Blalock, J. A. Hossack, and W. F. Walker, "Direct sampled I/Q beamforming for compact and very low-cost ultrasound imaging," *IEEE Trans. Ultrason., Ferroelectr., Freq. Control*, vol. 51, no. 9, pp. 1082–1094, Sep. 2004.
[77] B. E. Treeby and B. T. Cox, "K-Wave: MATLAB toolbox for the simulation and reconstruction of photoacoustic wave fields," *J. Biomed. Opt.*, vol. 15, no. 2, 2010, Art. no. 021314.
[78] M. T. Graham, R. A. Dunne, and M. A. L. Bell, "Comparison of compressional and elastic wave simulations for patient-specific planning prior to transcranial photoacoustic-guided neurosurgery," *J. Biomed. Opt.*, vol. 26, no. 7, Jul. 2021, Art. no. 076006.
[79] G. Pinton, G. E. Trahey, and J. J. Dahl, "Sources of image degradation in fundamental and harmonic ultrasound imaging using nonlinear, full-wave simulations," *IEEE Trans. Ultrason., Ferroelectr., Freq. Control*, vol. 58, no. 4, pp. 754–765, Apr. 2011.
[80] C. Demené *et al.*, "Spatiotemporal clutter filtering of ultrafast ultrasound data highly increases Doppler and fultrasound sensitivity," *IEEE Trans. Med. Imag.*, vol. 34, no. 11, pp. 2271–2285, Nov. 2015.
[81] P. Podvin and I. Lecomte, "Finite difference computation of traveltimes in very contrasted velocity models: A massively parallel approach and its associated tools," *Geophys. J. Int.*, vol. 105, no. 1, pp. 271–284, Apr. 1991.
[82] C. Demené *et al.*, "Transcranial ultrafast ultrasound localization microscopy of brain vasculature in patients," *Nature Biomed. Eng.*, vol. 5, no. 3, pp. 219–228, Mar. 2021.
[83] C. Robba and G. Citerio, *Echography and Doppler of the Brain*. Berlin, Germany: Springer, 2021.
[84] E. Mace, G. Montaldo, B. Osmanski, I. Cohen, M. Fink, and M. Tanter, "Functional ultrasound imaging of the brain: Theory and basic principles," *IEEE Trans. Ultrason., Ferroelectr., Freq. Control*, vol. 60, no. 3, pp. 492–506, Mar. 2013.
[85] H. Hasegawa and H. Kanai, "High-frame-rate echocardiography using diverging transmit beams and parallel receive beamforming," *J. Med. Ultrason.*, vol. 38, no. 3, pp. 129–140, 2011.
[86] G. Montaldo, M. Tanter, J. Bercoff, N. Benech, and M. Fink, "Coherent plane-wave compounding for very high frame rate ultrasonography and transient elastography," *IEEE Trans. Ultrason., Ferroelectr., Freq. Control*, vol. 56, no. 3, pp. 489–506, Mar. 2009.
[87] J. Baranger *et al.*, "Bedside functional monitoring of the dynamic brain connectivity in human neonates," *Nature Commun.*, vol. 12, no. 1, pp. 1–10, Dec. 2021.
[88] E. Macé, G. Montaldo, I. Cohen, M. Baulac, M. Fink, and M. Tanter, "Functional ultrasound imaging of the brain," *Nature Methods*, vol. 8, pp. 662–664, May 2011.

Moein Mozaffarzadeh received the B.Sc. degree in electrical engineering from the Babol Noshirvani University of Technology, Babol, Mazandaran, Iran, in 2015, and the M.Sc. degree in biomedical-bioelectric engineering from Tarbiat Modares University, Tehran, Iran, in 2017. He is currently pursuing the Ph.D. degree with the Laboratory of Medical Imaging, Department of Imaging Physics, Delft University of Technology, Delft, The Netherlands.

His research interests include photoacoustic/ultrasound imaging, acoustic beamforming, and medical ultrasound transducer design.

Dirk J. Eric Verschuur received the M.Sc. and Ph.D. (Hons.) degrees in applied physics from Delft University of Technology (DUT), Delft, The Netherlands, in 1986 and 1991, respectively.

He is currently an Associate Professor with the Department of Imaging Physics, DUT. Since 2016, he has been the Program Director of the Delphi Research Consortium, within which research is carried out in the area of geo-imaging. His main research interests are wavefield modeling, data processing, imaging and inversion techniques, and the use of machine learning for geo-imaging.

Dr. Verschuur received the SEG's J. Clarence Karcher Award in 1997 and the Virgil Kauffman Gold Medal from SEG in 2006.

Martin D. Verweij (Member, IEEE) received the M.Sc. (*cum laude*) and Ph.D. degrees in electrical engineering from Delft University of Technology, Delft, The Netherlands, in 1988 and 1992, respectively.

From 1993 to 1997, he was a Research Fellow with the Prestigious Royal Netherlands Academy of Arts and Sciences, Amsterdam, The Netherlands. In 1995 and 1997, he was a Visiting Scientist at Schlumberger Cambridge Research, Cambridge, U.K. In 1998, he became an Assistant Professor, and later an Associate Professor, with the Laboratory of Electromagnetic Research, Delft University of Technology, where he switched to the Laboratory of Acoustical Wavefield Imaging in 2011. Since 2015, he also has a part-time position at the Biomedical Engineering Group, Erasmus Medical Centre, Rotterdam, The Netherlands. His research interests include dedicated transducer design, beamforming algorithms, and the theoretical modeling and numerical simulation of medical ultrasound. He is the originator of the iterative nonlinear contrast source method for the computation of nonlinear ultrasound fields. He is the Research Leader of the Dutch Technology Foundation (STW) on projects involving transducer design, beamforming, and imaging.

Dr. Verweij was elected as the Best Teacher of the Electrical Engineering Curriculum in the academic year from 2001 to 2002. He is an Associate Editor of the *Journal of the Acoustical Society of America* and a Treasurer of the Dutch Society for Medical Ultrasound.

Nico de Jong (Member, IEEE) graduated from Delft University of Technology, Delft, The Netherlands, in 1978. He received the M.Sc. degree in physics (specialized in the field of pattern recognition) from Delft University of Technology, and the Ph.D. degree from the Erasmus Medical Center, Rotterdam, The Netherlands, in 1993. His Ph.D. dissertation was focused on acoustic properties of ultrasound contrast agents.

Since 1980, he has been a Staff Member with the Thorax Center, Erasmus Medical Center. In 2003, he was a part-time Professor with the Physics of Fluids Group, University of Twente, Enschede, The Netherlands. He teaches at technical universities and the Erasmus Medical Center. He has been a Promotor of 35 Ph.D. students and is currently supervising 11 Ph.D. students. Since 2011, he has been a Professor in molecular ultrasonic imaging and therapy with the Erasmus Medical Center and the Delft University of Technology.

Dr. de Jong is the Organizer of the Annual European Symposium on Ultrasound Contrast Imaging, held in Rotterdam and attended by approximately 175 scientists from universities and industries all over the world. He is on the Safety Committee of the World Federation of Ultrasound in Medicine and Biology. Over the last five years, he has given more than 30 invited lectures and has given numerous scientific presentations for international industries. He has been a guest editor for special issues of different journals. He is an Associate Editor of *Ultrasound in Medicine and Biology*.

Guillaume Renaud received the Engineering degree from ICAM Nantes, France, in 2004, the master's degree in acoustical physics from the University of Le Mans, France, in 2005, and the Ph.D. degree in biomedical physics from the University of Tours, Tours, France, in 2008.

After a Postdoctoral Fellowship at Erasmus MC, Rotterdam, The Netherlands, he was hired as a tenured scientist at CNRS, France, based within the Laboratory of Biomedical Imaging, Paris. His current research interests include nonlinear acoustics, imaging and quantification of intraosseous blood flow, and bone tissue properties with ultrasound.